Measurement of Vibration and Acoustic Noise Generated by Magnetostriction in Three Stator Cores Made of High Silicon Steel, Amorphous Iron, and Conventional Silicon Steel

Yifei Cai [1)] Akira Chiba [1)] Fares S. El-Faouri [1)] Naoki Saikawa [1)] Yoshizaki Soichiro [2)]

1) Electrical and Electronics Engineering Department
Tokyo Institute of Technology, Meguro, Tokyo, Japan
E-mail: cai.y@belm.ee.titech.ac.jp
2) Steel Research Laboratory
JFE Steel Corporation, Chiyoda, Tokyo, Japan
E-mail: s-yoshizaki@jfe-steel.co.jp

ABSTRACT: The deformation of stators due to radial electromagnetic forces is considered as the main source of vibration and acoustic noise in electric machines. Similarly, the deformation due to magnetostriction also contributes to the vibration and acoustic noise. In this paper, the magnetostrictive deformation, vibration, and sound pressure level are measured and compared with three stator cores. The three cores are made of high silicon steel, amorphous iron, and conventional silicon steel. These materials are selected for their significantly different magnetostriction properties. The measurement results indicate that magnetostriction can cause significant deformation, vibration, and acoustic noise.

KEY WORDS: magnetostriction, motor cores, vibration, acoustic noise

1. INTRODUCTION

In the electric-vehicle industry, electric machines with high efficiency, high torque density, and low NVH (noise, vibration, and harshness) are demanded. The electromagnetic forces periodically occurring on the stator teeth are considered to be the dominant source of vibration and acoustic noise. Furthermore, the force harmonics that coincide with the resonance frequencies of the machines result in severe acoustic noise(1). In electric-vehicle applications, the natural frequencies of the motor are lower due to a larger stator radius when compared with industrial ones with a few kW outputs(2). Consequently, it is difficult to avoid exciting the resonance modes at these natural frequencies within a wide operating speed range.

Approaches to reducing the vibration and acoustic noise in electric machines can be divided into two categories: mechanical structure improvement and control optimization. From the perspective of structure improvement, a step skewed rotor structure and stator structure with an extra bridge are proposed to optimize force characteristics and increase machine stiffness, respectively(3)(4). From the perspective of control optimization, current harmonic injection is proposed to reduce the force components exciting mode 0 natural resonance for the noise reduction in an interior permanent magnet synchronous machine (IPMSM)(5). Additionally, a numerical radial force shaping method is proved to be effective in reducing noise in switched reluctance machines (SRMs)(6)(7). In these methods, the contribution of magnetostriction to acoustic noise is not considered.

Magnetostriction in electromagnetic steel is the dominant source of vibration and acoustic noise in power transformers(8)(9). In electric machines, magnetostrictive deformation is also experimentally detected using strain gauges(10)(11). In (12), analysis results indicate that additional vibration occurs if magnetostriction is considered in an IPMSM. In reference (13), the sound pressure levels of three SRMs with an identical design but different core materials are measured, and the results indicate that cores with higher magnetostriction emit higher acoustic noise. In both reference (12) and (13), both electromagnetic force and magnetostriction simultaneously exist in the experiment and cause deformation; therefore, it is necessary to separate these two factors in order to investigate the contribution of magnetostriction solely to the vibration and acoustic noise in electric machines.

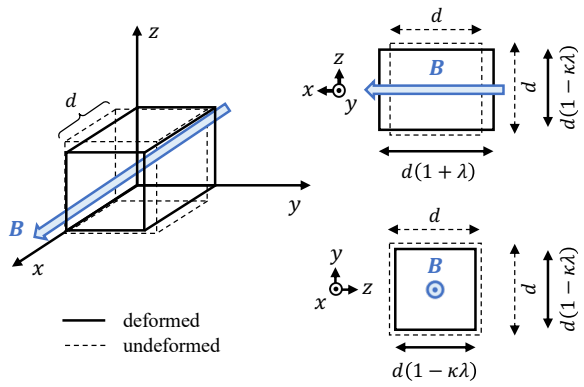

Fig. 1 Magnetostriction under the flux density aligned to x-axis. (a) A 3-dimensional view and (b) cross-sectional views.

In this paper, three stator cores made of different materials are excited by additional toroidal windings that constrain the flux inside the stator yoke, hence the occurrence of electromagnetic force is avoided, and the deformation is completely generated by magnetostriction. The three stator cores are designed for the motor used in automobiles and are made of three materials which are high silicon steel 10JNEX900, amorphous iron 2605SA1, and conventional silicon steel 20JNEH1200. These materials are selected for significantly different magnetostriction properties. These materials are selected in order to compare the strain, vibration, and sound pressure level resulting from different magnetostriction properties. Moreover, each core is excited in two ways: sinusoidal flux density excitation and square flux density excitation in the stator yoke with the aim of investigating the influence of magnetostriction harmonics on vibration and acoustic noise.

2. MAGNETOSTRICTION OF IRON MATERIAL

2.1. Analytical Expression of Magnetostriction

In this subsection, the MS tensor under a flux density vector aligned with the x-axis of the global Cartesian coordinate system is explained. Fig. 1 illustrates a cubic core with an initial edge length of d. The solid and dashed lines represent the core before and after MS deformation. As shown in the figure, the core is excited by a flux density $\boldsymbol{B}$ aligned with the x-axis, which is defined as

$$\boldsymbol{B} = [|\boldsymbol{B}| \quad 0 \quad 0]^T. \tag{1}$$

As shown in Fig. 1(b), the MS deformation causes tensile strain of λ in x-direction. As the cube is stretched along the x-axis, it is expected to be compressed in the other two directions, hence the tensile strains in y- and z-directions are defined as a negative value $-\kappa\lambda$. The tensile strains in y- and z-directions are equal owing to the material's isotropy assumption. Here, κ is the magnetostrictive Poisson's ratio that denotes the ratio of compression (negative strain) in the directions perpendicular to the magnetization. Fig. 1(b) displays two side views of the cube showing the expansion and compression in different directions.

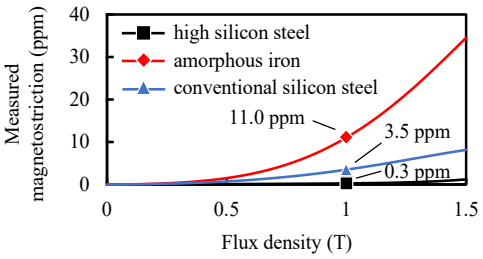

Fig. 2 Magnetostriction curves of three core materials.

The strain tensor based on infinitesimal strain theory is used to depict the strain on the core:

$$\epsilon_{ij} = \frac{1}{2}\left(\frac{\partial u_i}{\partial x_j} + \frac{\partial u_j}{\partial x_i}\right) \tag{2}$$

where x_i and u_i are the i-th material coordinate and the corresponding displacement of the cube shown in Fig. 1(b). Based on (2) and the deformation shown in Fig. 1(b), the MS strain tensor under the flux density given by (1) can be written as:

$$\Lambda = \begin{bmatrix} \lambda & 0 & 0 \\ 0 & -\kappa\lambda & 0 \\ 0 & 0 & -\kappa\lambda \end{bmatrix} \tag{3}$$

2.1. Magnetostriction Characteristics of the Core Materials

In this paper, three stator cores are fabricated with three electromagnetic steel materials: the high silicon steel 10JNEX900, amorphous iron 2605SA1, and conventional silicon steel 20JNEH1200. These materials have significantly different magnetostriction characteristics as shown in Fig. 2. These characteristics are measured by strain gauges at closed-loop laminated cores. The high silicon steel and amorphous iron have the lowest and highest magnetostriction, respectively, whereas that of the conventional silicon steel lies between the two materials. Under the identical excitation of 1 T, the magnetostriction values of the amorphous iron and conventional silicon steel are approximately 37 times and 12 times higher than that of the high silicon steel.

2.2. Stator Cores and Windings

Fig. 3(a) shows the experiment setup. The three stator cores have an identical structure originally designed for generators in

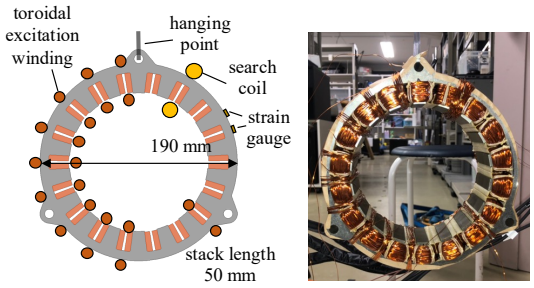

Fig. 3 (a) Stator core, windings, and fixation. (b) Hanged stator core with a toroidal excitation winding and search coil.

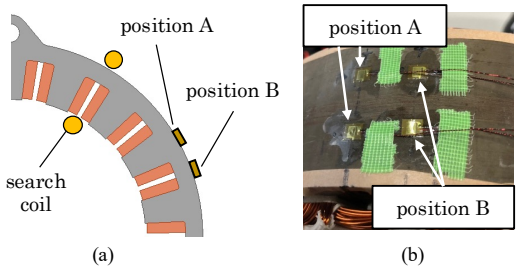

Fig. 5 (a) Installation position of the strain gauges. (b) Picture of installed strain gauges on the stator yoke.

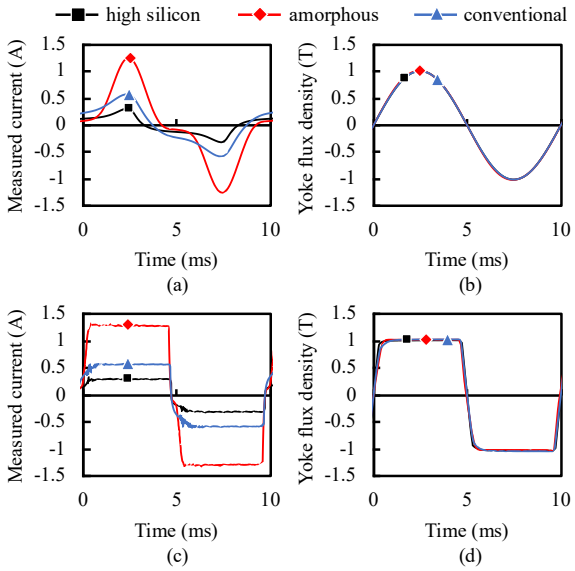

Fig. 4 (a) Measured excitation currents and (b) flux densities under 100-Hz sinusoidal flux density exitation. (c) Measured excitation currents and (d) flux densities under 100-Hz square flux density excitation.

hybrid electric vehicles. The outer diameter is 190 mm, and the stack length is 50 mm. In the experiment, the stator is hanged by a wire through the top ear by a crane. On the stator, a toroidal excitation winding of 100 turns is evenly distributed on 10 slots as shown in Fig. 3(a). The excitation winding is not wound over the entire stator yoke because of the installed strain gauges which are fragile to pressure. Additionally, a search coil of 50 turns is wound at the right-top of the core for flux detection. Fig. 3(b) is the picture of the stator hanged in the experiment with a toroidal excitation winging and search coil.

2.2. Core Excitation

In this paper, each stator core is excited by two excitations, sinusoidal and square flux density excitations in the stator yoke, for different purposes. Fig. 4 shows the measured current and yoke flux density waveforms at 100 Hz under the two flux density excitation patterns.

Under the current excitation shown in Fig. 4(a), the flux density generated inside the yoke varies sinusoidally as shown in Fig. 4(b). The current waveforms in Fig. 4(a) are not sinusoidal because of the magnetic saturation in the cores Under this sinusoidal flux density excitation, vibration and acoustic noise generated by the fundamental flux density component are measured and compared among the three materials at each excitation frequency (from 25 Hz to 1 kHz).

Under the current excitation shown in Fig. 4(c), the flux density in the stator yoke varies in a square shape as shown in Fig. 4(d). Since the square waveforms contain a considerable number of harmonics, the vibration and acoustic noise generated by the high-order harmonics are measured and compared.

In Figs. 4(b) and (d), the peaks of the flux density are controlled to be approximately 1 T at all excitation frequencies. Consequently, the waveforms of the excitation current are different as shown in Figs. 4(a) and (c) due to the different B-H curves of the three materials. It is noteworthy that the flux densities shown in Figs. 4(b) and (c) are those that distribute in the yoke between the teeth instead of the yoke immediately behind the teeth.

3. MEASUREMENT OF STRAIN, VIBRATION, AND SOUND PRESSURE LEVEL

3.1. Strain Measurement

The magnetostriction occurring on the outer surface of the stator core is measured by strain gauges. A strain gauge detects the local mechanical deformations and converts them into electrical signals. It is directly attached to a target and deforms together when the target is deformed by external or internal stress.

Fig. 5(a) shows the two positions where strain gauges are installed. Position A is immediately behind a stator tooth, and position B is at the middle point of the yoke between two teeth.

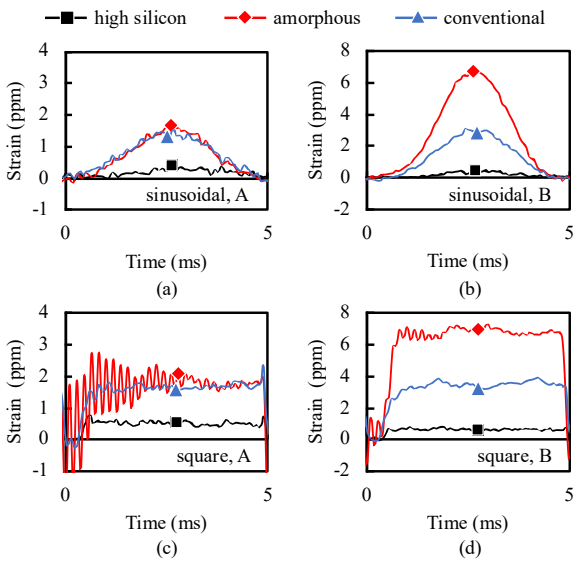

Fig. 6 Strain gauge outputs under 1-kHz sinusoidal flux density exitation at (a) position A and (b) position B.
Strain gauge outputs under 1-kHz square flux density exitation at (c) position A and (d) position B.

These two positions can sufficiently represent the strain on the entire stator due to its symmetry. Fig. 5(b) is the picture of the stator yoke outer surface on which four strain gauges are attached. At each position, A and B, a pair of strain gauges is installed. The two strain gauges at each position detect the identical strain owing to their equivalent position with respect to the stack direction. The respective average of each strain gauge pair is adopted in order to increase the signal-to-noise ratio.

Figs. 6(a) and (b) show the half cycles of the measured strains at positions A and B, respectively, under sinusoidal flux density excitation at 100 Hz. In both Figs. 6(a) and (b), the measured strains of the three cores are positive, which indicates that an expansion occurs on the core outer surface under excitation. Furthermore, the shapes of strain waveforms correspond to that of the flux density waveforms shown in Fig. 4(b). However, the strain waveforms are not perfectly sinusoidal because of the non-linear relationships between the magnetostriction and flux density shown in Fig. 2. When comparing the strain amplitudes among the materials, both gauges in position A and position B detect the highest strains in the amorphous iron and the lowest strains in the high silicon steel as shown in Figs. 6(a) and (b). This result corresponds to the order of the magnetostriction amplitudes shown in Fig. 2. When comparing the difference in the strains measured at position A and position B, it is noteworthy that the scale of the vertical axis in Fig. 6(b) is two times larger than that in Fig. 6(a); therefore, the strain detected at position B is much higher than that

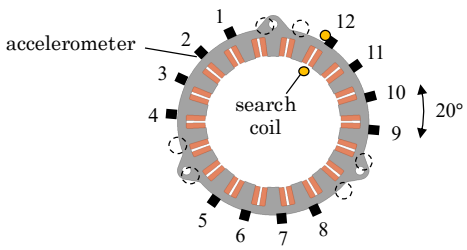

Fig. 7 Installation position of the accelerometers.

detected at position A. These results are caused by the difference in flux density at the two positions. A part of the flux passes through the tooth beneath position A, while all the flux concentrates in the yoke beneath position B. Thus, the flux density beneath position A is lower and leads to a smaller magnetostrictive expansion.

Figs. 6(c) and (d) show the measured strains at position A and position B, respectively, under the square flux density excitation. Most characteristics of the strain waveforms are similar to those under the sinusoidal flux density excitation, except for the shape. The square shapes of the strain waveforms correspond to those of the flux density waveforms shown in Fig. 6(d), which indicates the rapid shape deformation of the stator under the square flux density excitation.

From the measured strains shown in Fig. 6, it can be concluded that expansion is caused by the magnetostriction in a magnetized core. Moreover, larger expansion occurs in the materials with higher magnetostriction.

3.2. Vibration Measurement

Twelve synchronized accelerometers are installed around the stator yoke to measure the radial vibration. Fig. 7 shows the positions of the accelerometers on the core. Except for the six positions near the three ears, all the accelerometers are distributed with a 20-degree interval. These synchronized sensors can measure both the amplitude and the mode shape of the vibration.

Figs. 8(a) and (b) show the comparison of the vibration among the three materials under 1-kHz sinusoidal and square flux density, respectively. The average of all twelve accelero-meter signals is adopted for comparison because all the signals have good agreement with each other. Under both the sinusoidal and square flux density excitations, the amorphous iron core and high silicon steel core show the highest and lowest vibration, respectively. The correspondence between the order of vibration amplitude and the material magnetostriction shown in Fig. 1(b) indicates that materials with higher magnetostriction show more intensive vibration.

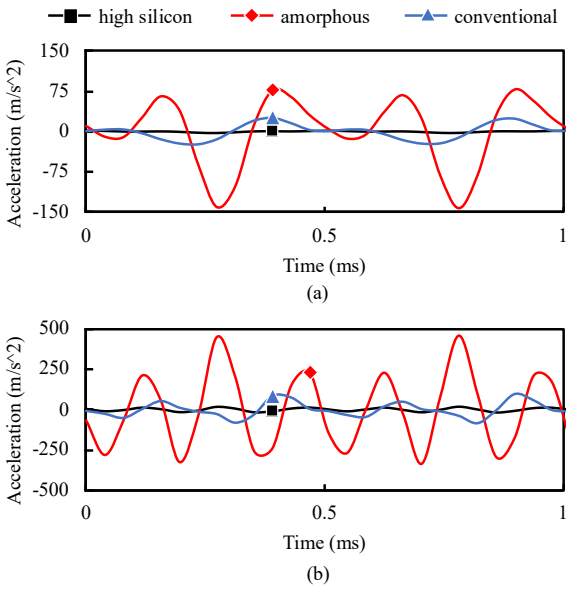

Fig. 8 Average accelerations in time domain under 1-kHz (a) sinusoidal flux density and (b) square flux density.

When compared with the vibration under the sinusoidal flux density in Fig. 8(a), the vibrations in the three cores are all higher under the squared flux density as shown in Fig. 8(b) This is due to the fact that the magnetostriction generated under the square flux density contains numerous harmonics with significantly high amplitudes. Additionally, six peaks are observed within one period (1 ms) in the high silicon steel and amorphous iron cores; in other words, the frequencies of the dominant component are six times the fundamental frequency of 1 kHz; which is at 6 kHz. In these two materials, the 6th harmonics of the excitation, that is 6 kHz, coincides with the natural frequency of mode 0 of the cores and consequently excites significant vibrations. In the case of the conventional silicon steel core, the mode 0 resonance is at approximately 4 kHz since its vibration has four peaks within one period in Fig. 8(b).

3.2. Vibration Measurement

The sound pressure level (SPL) due to magnetostrictive vibration is measured by a microphone set 1 m away from the stator yoke. The SPLs under the sinusoidal and square flux density excitations are summarized in the Campbell diagrams in Fig. 9 and Fig. 10, respectively. The excitation frequency ranges from 25 Hz to 1 kHz (25-Hz interval), and the SPL frequency ranges from 0 Hz to 8 kHz.

In all the diagrams, the trajectories of the harmonics can be clearly observed, and the order of each trajectory is highlighted in Fig. 9(a) and Fig. 10(a). As shown in the diagrams, all the trajectories are the multiples of the second harmonic of the excitation. The reason is that magneto-striction depends on only the amplitude of flux density in non-oriented materials. Therefore, in Figs. 4(b) and (d), the first and second halves of the flux density waveform result in an identical magnetostriction waveform. Consequently, magnetostriction has double the frequency of the excitation.

In Fig. 9, the highest SPL point is highlighted in red for each material. They are 56 dB, 83 dB, and 76 dB in the high silicon steel, amorphous iron, and conventional silicon steel core, respectively. The highest SPLs correspond to the order of material magnetostriction shown in Fig. 2. Furthermore, the highest SPL appears on the trajectory of the 2nd harmonic in all cores because they are excited under sinusoidal flux density with a dominant fundamental component and limited harmonics. However, the harmonics with higher order also appear on the diagrams due to the non-linear relationship between magnetostriction and flux density as shown in Fig. 2. The highest SPLs on the 4th harmonic trajectories are highlighted in Fig. 9 and are much smaller than those on the 2nd harmonic trajectories.

Fig. 10 shows Campbell diagrams under the square flux density excitation. Compared to those in Fig. 9, the SPLs in Fig. 10 are significantly higher. Additionally, not only the 2nd harmonic trajectory but those which are the multiples of the 2nd harmonic are also clearly depicted, such as the 8th harmonic trajectories which can be clearly seen in Figs. 10(a) and (c) but hardly observed in Figs. 9 (a) and (c). These are due to the high harmonic components contained in the square flux density excitation.

In Fig. 10, the SPL values corresponding to those highlighted in Fig. 9 are also highlighted in order to compare the SPLs at each harmonic trajectory under different flux density excitations. Firstly, let us compare the SPLs on the 2nd harmonic trajectories. The SPLs on the 2nd harmonic trajectories are similar between the cases of the sinusoidal and square flux density excitations because the amplitudes of the fundamental component in flux density are similar. For instance, when comparing the highlighted SPLs on the 2nd trajectory in Figs. 9 and 10, the highlighted SPLs are 56 dB and 58 dB in the high silicon steel, 83 dB and 84 dB in the amorphous iron, and 76 dB and 75 dB in the conventional silicon steel. Secondly, let us discuss the SPLs on the 4th harmonic trajectories. Due to the numerous harmonics with high amplitude in the square flux density excitation, a significant difference from the sinusoidal flux density excitation is observed. For instance, the highlighted SPLs at the 4th harmonic trajectory under the two flux density excitations are 29 dB and 54 dB in the high silicon steel,

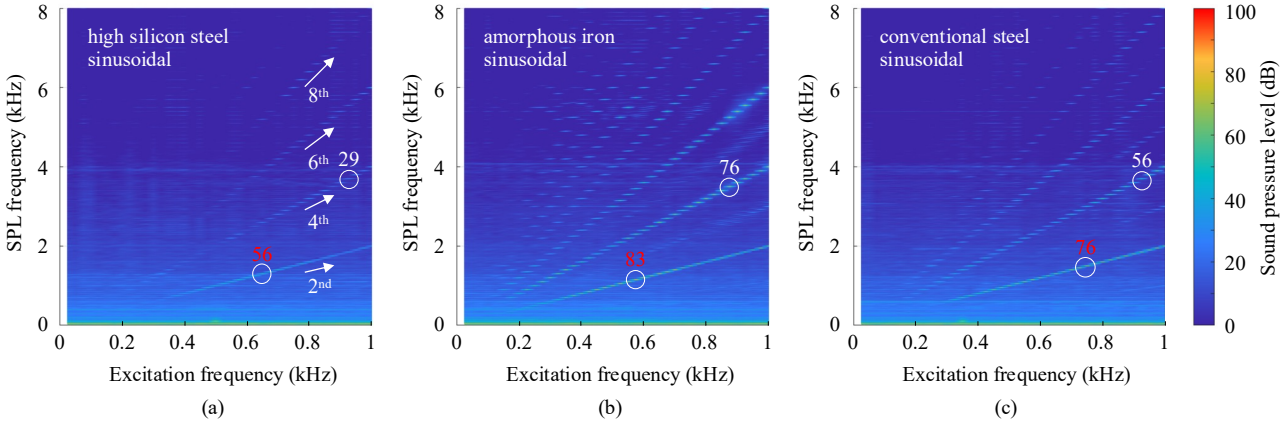

Fig. 9. Campbell diagrams of (a) high silicon steel, (b) amorphous iron, and (c) conventional silicon steel cores under sinusoidal flux density exitation.

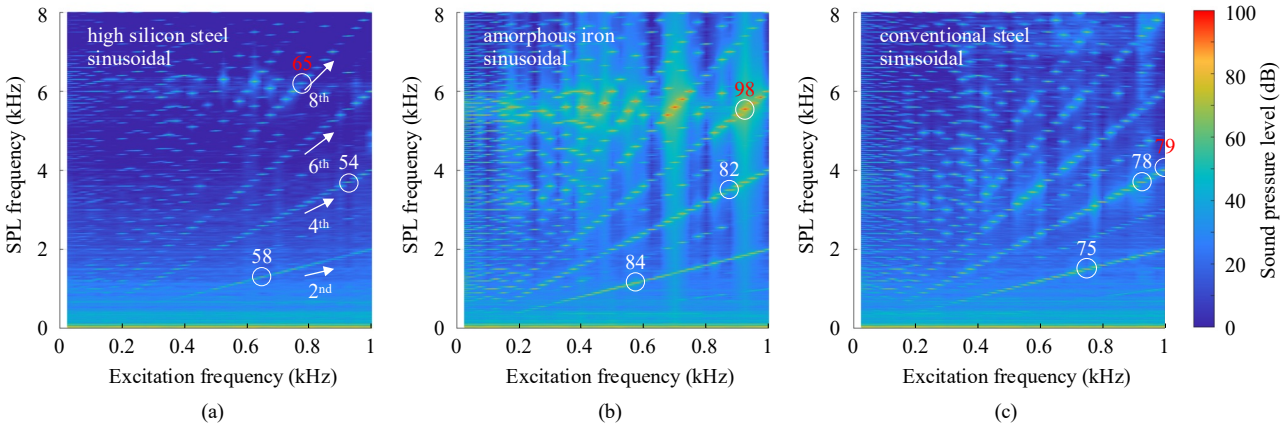

Fig. 10. Campbell diagrams of (a) high silicon steel, (b) amorphous iron, and (c) conventional silicon steel cores under square flux density excitation.

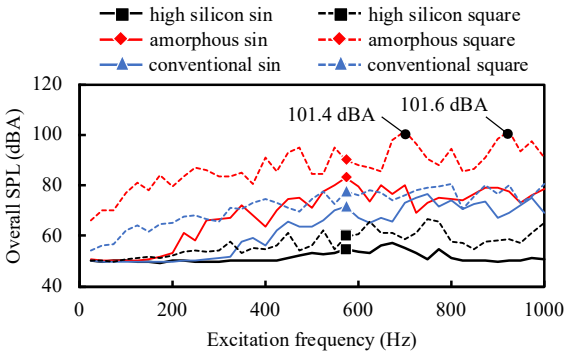

Fig. 11 Comparison of the overall SPL in the three materials under sinusoidal and square flux density excitations.

76 dB and 82 dB in the amorphous iron, and 56 dB and 78 dB in the conventional silicon steel. These values are significantly higher under the square flux density excitation. Moreover, the highest SPLs are highlighted in red in Fig. 10, and these highest SPLs are not on the 2nd harmonic trajectories as those shown in Fig. 9. The highest SPLs are 65 dB, 98 dB, and 79 dB at the 8th, 6th, and 4th harmonic trajectories in the high silicon steel, amorphous iron, and conventional silicon steel, respectively. The reason is that, in each core, the respective trajectory coincides with the natural frequency of mode 0 and excites the mode 0 resonance. In Figs. 10(a) and (b), two significantly high SPLs bands are observed around the SPL frequency around 6 kHz in the high silicon steel and amorphous iron. In the case of the conventional silicon steel, the band is around 3.8 kHz.

Fig. 11 shows a comparison of the overall A-weighted SPL based on the Campbell diagrams shown in Fig. 9 and Fig. 10. The SPLs in solid lines and dashed lines represent those measured under sinusoidal and square flux density excitations, respectively. Firstly, as shown in Fig. 11, the overall SPLs of the high silicon steel and amorphous iron core are the lowest and the highest at most excitation frequencies among either the solid line group or the dashed line group. The order of the SPL corresponds to the order of material magnetostriction when the cores are under the same flux density excitation. Secondly, the dashed overall SPLs are always higher than the solid ones in all three materials, which indicates that the square flux density always results in higher SPLs than the sinusoidal one. From this difference, it can be concluded that it is possible to reduce SPL by properly regulating the

magnetostriction that occurs in the stator yoke. Moreover, the two peaks in the overall SPL plot measured from the amorphous iron core under square flux density excitation reach 101.4 dB at 700 Hz and 101.6 dB at 925 Hz, which are extremely high SPLs and harmful to human hearing. The peak overall SPLs measured from the conventional silicon steel and high silicon steel are 80.6 dB and 65.6 dB, respectively. The results shown in Figs. 9 to 11 indicate that magnetostriction significantly contributes to the acoustic noise. Additionally, it is found that the stator cores made of materials with higher magnetostriction generate higher SPLs.

4. CONCLUSION

In this paper, three stators made of core materials with significantly different magnetostriction characteristics are tested. The diameter of the stators is 190 mm, which is identical to the generator used in a hybrid electric vehicle. The strain, vibration, and sound pressure level (SPL) due to the magnetostriction occurring under sinusoidal and square flux density excitations are compared. From the measured strain results, it can be concluded that magnetostriction causes expansion in the cores under excitation. Moreover, the outputs of accelerometers indicate that the vibration is dominantly in the shape of mode 0. It is also found that materials with higher magnetostriction result in higher expansion, vibration, and SPL. Furthermore, square flux density with numerous high harmonics excites more intensive vibration and higher SPL in all three materials. Under square flux density excitation, significantly high SPL is measured when the mode 0 resonance is excited by the high-order harmonics. The peak overall SPLs in the amorphous iron and conventional silicon steel are as high as 101.6 dB and 80.6 dB, respectively. On the other hand, the peak overall SPL in the high silicon steel is lower, that is 65.6 dB, due to its low magnetostriction characteristic.

ACKNOWLEDGMENT

The authors would like to thank ANSYS Inc. for their support on ANSYS software. The authors would also like to thank JFE Corporation for their support on core fabrication.

REFERENCES

(1) D. E. Cameron, J. H. Lang and S. D. Umans, "The origin and reduction of acoustic noise in doubly salient variable-reluctance motors," in IEEE Transactions on Industry Applications, vol. 28, no. 6, pp. 1250-1255, Nov.-Dec. 1992.

(2) J. Hong, S. Wang, Y. Sun and H. Cao, "A Method of Modal Parameter Estimation of the Motor Based on Electromagnetic Vibration Exciter," in IEEE Transactions on Industry Applications, vol. 56, no. 3, pp. 2636-2643, May-June 2020.

(3) J. -W. Jung, D. -J. Kim, J. -P. Hong, G. -H. Lee and S. -M. Jeon, "Experimental Verification and Effects of Step Skewed Rotor Type IPMSM on Vibration and Noise," in IEEE Transactions on Magnetics, vol. 47, no. 10, pp. 3661-3664, Oct. 2011.

(4) S. Das, O. Gundogmus, Y. Sozer, J. Kutz, J. Tylenda and R. L. Wright, "Wide Speed Range Noise and Vibration Mitigation in Switched Reluctance Machines With Stator Pole Bridges," in IEEE Transactions on Power Electronics, vol. 36, no. 8, pp. 9300-9311, Aug. 2021.

(5) S. Ciceo, F. Chauvicourt, J. Gyselinck and C. Martis, "PMSM Current Shaping for Minimum Joule Losses While Reducing Torque Ripple and Vibrations," in IEEE Access, vol. 9, pp. 114705-114714, 2021.

(6) M. Takiguchi, H. Sugimoto, N. Kurihara and A. Chiba, "Acoustic Noise and Vibration Reduction of SRM by Elimination of Third Harmonic Component in Sum of Radial Forces," in IEEE Transactions on Energy Conversion, vol. 30, no. 3, pp. 883-891, Sept. 2015.

(7) A. D. Callegaro, B. Bilgin and A. Emadi, "Radial Force Shaping for Acoustic Noise Reduction in Switched Reluctance Machines," in IEEE Transactions on Power Electronics, vol. 34, no. 10, pp. 9866-9878, Oct. 2019.

(8) M. Liu, O. Hubert, X. Mininger, F. Bouillault, L. Bernard and T. Waeckerlé, "Reduction of Power Transformer Core Noise Generation Due to Magnetostriction-Induced Deformations Using Fully Coupled Finite-Element Modeling Optimization Procedures," in IEEE Tran-sactions on Magnetics, vol. 53, no. 8, pp. 1-11, Aug. 2017.

(9) R. Ricardo et al., “Study of Transformer Core Vibration and Noise Generation Mechanism Induced by Magnetostriction of Grain-Oriented Silicon Steel Sheet,” in Shock and Vibration, vol. 2021, no. 8850780, 2021.

(10) Y. Cai, H. Sobue, C. A. Wiguna, A. Chiba, K. Senda and S. Yoshizaki, "Analytical and Experimental Investigations of Magnetostriction Influence on Strain Measurement in Switched Reluctance Machines," 2021 IEEE Energy Conversion Congress and Exposition (ECCE), 2021, pp. 4436-4442.

(11) S. Somkun, A. J. Moses and P. I. Anderson, "Effect of Magnetostriction Anisotropy in Nonoriented Electrical Steels on Deformation of Induction Motor Stator Cores," in IEEE Transactions on Magnetics, vol. 45, no. 10, pp. 4744-4747, Oct. 2009.

(12) L. Zhu, B. Wang, R. Yan, Q. Yang, Y. Yang and X. Zhang, "Electromagnetic Vibration of Motor Core Including Magnetostriction Under Different Rotation Speeds," in IEEE Transactions on Magnetics, vol. 52, no. 3, pp. 1-4, March 2016.

(13) H. Sobue et al., "Analysis and Experimental Comparison of Acoustic Noise of Three Switched Reluctance Motors Made of Conventional Steel, High Silicon Steel, and Amorphous Iron," in IEEE Transactions on Industry Applications, vol. 57, no. 6, pp. 5907-5915, Nov.-Dec. 2021.